Biophysical Reports

ARTICLE

Calibration-free counting of low molecular copy numbers in single DNA-PAINT localization clusters

Johannes Stein,[1] Florian Stehr,[1] Ralf Jungmann,[1,2] and Petra Schwille[1,*]
[1]Max Planck Institute of Biochemistry, Martinsried, Germany and [2]Faculty of Physics, Ludwig Maximilian University, Munich, Germany

ABSTRACT Single-molecule localization microscopy (SMLM) has revolutionized light microscopy by enabling optical resolution down to a few nanometer. Yet, localization precision commonly does not suffice to visually resolve single subunits in molecular assemblies or multimeric complexes. Because each targeted molecule contributes localizations during image acquisition, molecular counting approaches to reveal the target copy numbers within localization clusters have been persistently proposed since the early days of SMLM, most of which rely on preliminary knowledge of the dye photophysics or on a calibration to a reference. Previously, we developed localization-based fluorescence correlation spectroscopy (lbFCS) as an absolute ensemble counting approach for the SMLM-variant DNA-PAINT (points accumulation for imaging in nanoscale topography), for the first time, to our knowledge, circumventing the necessity for reference calibrations. Here, we present an extended concept termed lbFCS+, which allows absolute counting of copy numbers for individual localization clusters in a single DNA-PAINT image. In lbFCS+, absolute counting of fluorescent loci contained in individual nanoscopic volumes is achieved via precise measurement of the local hybridization rates of the fluorescently labeled oligonucleotides ("imagers") employed in DNA-PAINT imaging. In proof-of-principle experiments on DNA origami nanostructures, we demonstrate the ability of lbFCS+ to truthfully determine molecular copy numbers and imager association and dissociation rates in well-separated localization clusters containing up to 10 docking strands. For $N \leq 4$ target molecules, lbFCS+ is even able to resolve integers, providing the potential to study the composition of up to tetrameric molecular complexes. Furthermore, we show that lbFCS+ allows resolving heterogeneous binding dynamics, enabling the distinction of stochastically generated and a priori indistinguishable DNA assemblies. Beyond advancing quantitative DNA-PAINT imaging, we believe that lbFCS+ could find promising applications ranging from biosensing to DNA computing.

WHY IT MATTERS Fluorescence microscopy is a powerful technology for life science and medical research because of its ability to look at specific targets within cells and tissues. Over the past two decades, the invention of super-resolution microscopy has enabled researchers to push the achievable resolution of fluorescence microscopy to the nanoscale. Yet, this resolution is not sufficient to routinely resolve individual biomolecules as building blocks of hierarchical structures and complexes, which is key for a deeper understanding of molecular biology. Here, we propose a strategy for the super-resolution microscopy technique DNA-PAINT that enables absolute counting of target molecules even in optically unresolvable molecular assemblies. Hence, our approach, termed lbFCS+, might become a useful tool for biological discovery at the nanoscale.

INTRODUCTION

The advent of super-resolution (SR) microscopy has revolutionized life science research by allowing the visualization of specific biological structures at the nanoscale (1–4). The SR methods summarized as single-molecule localization microscopy (SMLM), such as photoactivated localization microscopy (PALM) (3), stochastic optical reconstruction microscopy (STORM) (4), and (DNA)-points accumulation for imaging in nanoscale topography (PAINT) (5–7) circumvent the diffraction limit by acquiring image sequences of a "blinking" target structure by stochastically activating only a small subset of all fluorescent labels at a time. Thus, these methods enable localization of individual dye molecules in each camera frame and downstream

Submitted August 30, 2021, and accepted for publication November 4, 2021.

*Correspondence: schwille@biochem.mpg.de

Johannes Stein and Florian Stehr contributed equally to this work.

Editor: Jörg Enderlein.

https://doi.org/10.1016/j.bpr.2021.100032

rendering of SR images from all obtained localizations. However, the limited photon budgets of dyes (8), imperfect labeling strategies, and the physical size of the label (e.g., antibodies) cause these localizations to be scattered around the true position of the targeted molecule (forming a "localization cluster") (9). Within fixed cells, single molecules can thus only be pinpointed at lateral localization precisions of up to 10 nm (10), which is often not sufficient to reach molecular resolution and visually resolve molecular complexes. To give an example, it is not possible to visually distinguish the two monomers within a dimer, because the localizations obtained from both molecules overlap within a localization cluster. However, because in SMLM each targeted molecule contributes a certain number of localizations to the SR image, a quantitative analysis of the collected localizations from a specific (nanoscopic) volume in principle allows inferring back on the hidden number of targeted molecules within this volume (11).

Based on this concept, there have been a multitude of studies dedicated to the problem of "molecular counting" since the early beginnings of SMLM, especially for the methods PALM and STORM (12–26). While the required single-molecule blinking in PALM is achieved by light-induced stochastic photoactivation and subsequent photobleaching of the fluorophores (3,27), STORM exploits the light-induced photoswitching of fluorophores between a fluorescent bright state and a nonfluorescent dark state (4,28). Hence, for both methods, the success of a quantitative analysis of localization clusters critically depends on an exact photophysical modeling of the specific system with respect to photobleaching (29), intrinsic and/or extended blinking (12,14,20), and photoquenching (25) of the fluorophores in use.

In contrast to direct and permanent dye labeling as used in STORM and PALM, DNA-PAINT exploits the transient hybridization of short single-stranded and fluorescently labeled DNA probes ("imagers") to their complementary "docking strands" attached as labels to the target molecules (6,7). Because the required blinking is generated by the stochastic imager-docking strand binding reaction, DNA-PAINT is largely independent of the photophysical properties of fluorophores under appropriate experimental conditions (e.g., sufficiently low excitation intensities to reduce any residual photobleaching or the permanent photo-induced damage of docking strands) (7,30–32). In this case, localization clusters in DNA-PAINT data offer a unique potential for a quantitative interpretation, as the underlying bimolecular hybridization reaction between imager and docking strands is highly programmable and well-understood (11,25,33). In fact, an approach termed quantitative PAINT has been successfully used for molecular counting in localization clusters by using the imager influx rate as a calibration (34).

So far, all of the approaches to the problem of molecular counting in any of the SMLM variants were based on either 1) a priori knowledge of the blinking dynamics or the number of localizations per fluorescence marker (e.g., via supplementary experiments or theoretical modeling) or 2) on an initial calibration directly within the sample by using isolated localization clusters originating from an assumed number of fluorescent molecules as a reference. Hence, those approaches only allow relative counting compared to a reference sample or given by the model assumptions.

In a previous study, we introduced an approach termed localization-based fluorescence correlation spectroscopy (lbFCS) that allows absolute molecular counting in localization clusters in DNA-PAINT images, without the need of a separate reference measurement and using only minimal theoretical assumptions (32). However, lbFCS required at least two measurements of the same sample at distinct and correctly adjusted imager concentrations, making an experiment rather tedious and time consuming. Additionally, lbFCS could only yield average values for both the underlying hybridization rates and the counted copy numbers and was hence not suited for the detection of possible heterogeneities between clusters. Finally, since its first implementation, several studies have worked on the "speed up" of the DNA-PAINT reaction (10,35–37), promising benefits on the achievable statistics (e.g., more binding events can now be recorded in the same amount of time).

Overcoming these limitations, we present here a revised framework lbFCS+, which allows the extraction of absolute molecular numbers and hybridization rates of single DNA-PAINT clusters requiring only a single DNA-PAINT image acquisition. In proof-of-principle experiments on DNA origami nanostructures (38), we demonstrate the ability of lbFCS+ to truthfully determine molecular copy numbers and dissociation and association rates k_{off} and k_{on} of the imager-docking strand reaction in well-separated localization clusters containing up to six docking strands. We further thoroughly assess its applicable working range for reliable counting, which is largely determined by the experimentally used imager concentrations and image acquisition length. Using lbFCS+, we observe changes in the imager and docking strand binding dynamics solely induced by placing docking strands at different positions of the DNA origami. Exploiting this effect, we are able to resolve heterogeneous binding dynamics within individual DNA-PAINT clusters, allowing for the distinction of

stochastically generated and a priori indistinguishable DNA assemblies.

MATERIALS AND METHODS

Brief recap of SMLM and DNA-PAINT binding dynamics

This section reviews the fundamental principles of DNA-PAINT binding kinetics, which constitute the basis of lbFCS+. For a detailed description of the working principles of SMLM in general and DNA-PAINT in particular, the reader is referred to (33) and (7), respectively.

A DNA-PAINT experiment (6,7) is characterized by the transient binding reaction of short fluorescently labeled DNA oligonucleotides in solution ("imager strands," short: "imagers") to complementary "docking strands," which are attached as labels to the target molecules of interest (see schematic in Fig. 1 *a*). At a given imager concentration *c* (typically on the order of ~10 nM), the binding and unbinding reaction between imagers and docking strands is governed by the association rate k_{on} and the dissociation rate k_{off}. Although the dissociation reaction is a zero-order chemical reaction and thus independent of the reactant concentrations, the association reaction leading to the formation of the docking and imager strand duplex is a first-order chemical reaction. Because of the "infinite reservoir" of imagers in solution, their concentration can be assumed to be constant during DNA-PAINT image acquisition. This leads to a constant effective association rate $\tilde{k}_{on} \equiv k_{on}c$ dependent on the imager concentration.

The schematic in Fig. 1 *a* depicts *N* docking strands spaced at only a few nanometers because of an exemplary local assembly of target molecules within the sample. During image acquisition, the "blinking" raw signal recorded over time from this position consists of a series of bright frames (at least one imager strand bound to any of the *N* docking strands) and dark frames (no imager strand bound to any of the *N* docking strands), as illustrated in Fig. 1 *b*. As is common for SMLM, the raw signal is converted into a list of localizations during postprocessing, commonly referred to as SR reconstruction. This is achieved by fitting a two-dimensional Gaussian function to each of the identified diffraction limited spots, thereby pinpointing the fluorophore's center coordinates (i.e., localization; *red dots* in Fig. 1 *b*). An exemplary list of localizations as obtained from the *N* docking strands by this procedure is shown in Fig. 1 *c*. Each localization carries information about the *x* and *y* coordinates of the identified spot (i.e., its spatial information) and a time stamp *t* of its occurrence as well as the total amount of recorded photoelectrons *I*(*t*) contained within the spot (i.e., its temporal intensity information). The spatial information contained in this list can be used to reconstruct a SR image from our exemplary molecular assembly in form of a *x*-*y* scatter plot

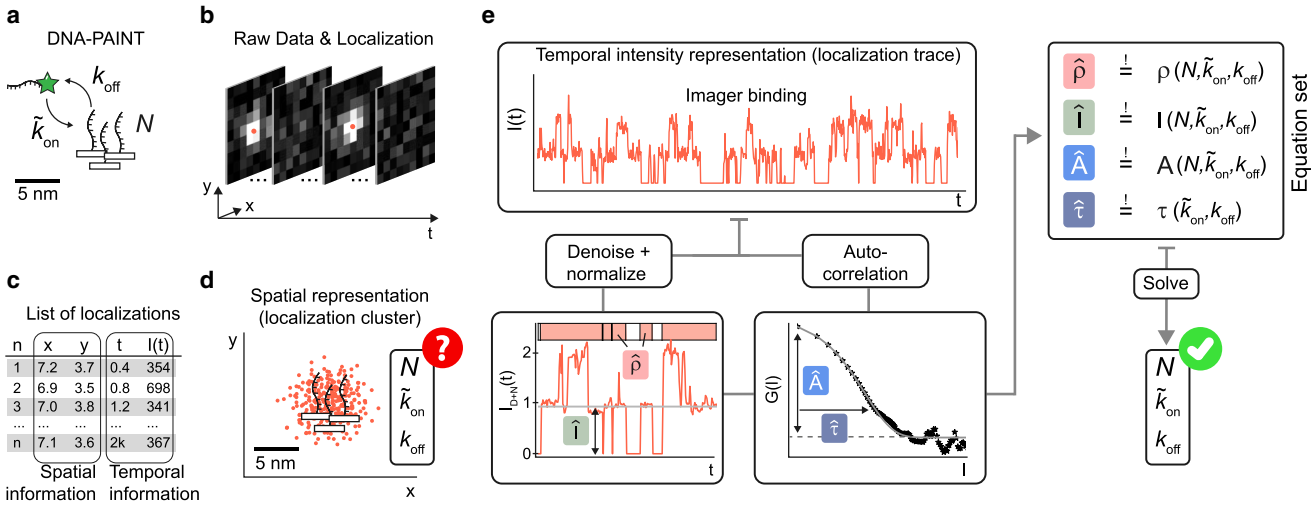

FIGURE 1 Absolute counting of molecular copy numbers in a single DNA-PAINT experiment. (*a*) Schematic of DNA-PAINT. The transient binding of fluorescently labeled imager strands to complementary docking strands attached to the target molecules of interest is shown. The binding reaction is governed by reaction rates k_{off} and $\tilde{k}_{on}$. Multimeric organization of the target molecules can lead to accumulations of *N* docking strands at very close spacing (<5 nm). (*b*) Sparse transient imager binding ensures the detection of single-molecule fluorescence signals during data acquisition of typically several thousand frames. Fitting the center coordinates of each single-molecule detection during postprocessing allows obtaining a localization that pinpoints the actual position of the underlying docking strand at nanometer precision (*red points*). (*c*) A processed DNA-PAINT data set consists of a list that contains all n obtained localizations (typically on the order of 10^6). Each localization is associated to accessible quantities such as its spatial coordinates (*x*, *y*; in case of a two-dimensional image), the frame *t* in which it was localized, and its intensity *I*(*t*) as the number of detected photoelectrons. (*d*) An *x*-*y* scatter plot allows rendering a SR image as the spatial representation of the localization list (*red dots*). Ideally, the position of each docking strand is revealed by a clearly distinguishable localization cluster. In case of multimeric targets, however, localizations obtained from multiple tightly spaced docking strands can overlap in a nonresolvable localization cluster in the DNA-PAINT image. We are asking the question whether it is possible to derive the unknown physical quantities *N*, $\tilde{k}_{on}$, and k_{off} based on a single localization cluster, but for all localization clusters contained in the overall DNA-PAINT image. (*e*) The starting point of our solution to this problem is the intensity versus time information that is associated to each localization cluster (compare *c*). This "intensity trace" contains the temporal intensity fluctuations due to imager binding and unbinding that were detected from the position of the localization cluster during data acquisition. The intensity trace of each localization cluster is subject to two parallel analysis work streams (see The analysis approach of lbFCS+ for detailed description): 1) denoising and normalization, which yields the two observables mean intensity $\hat{I}$ and occupancy $\hat{\rho}$ of the intensity trace, as well as 2) autocorrelation analysis, which yields the two observables amplitude $\hat{A}$ and decay constant $\hat{\tau}$ of the computed autocorrelation curve. Lastly, the four observables $\hat{\rho}$, $\hat{I}$, $\hat{A}$, and $\hat{\tau}$ are inputted to a least-square optimization of a defining set of equations to find a solution for the unknowns *N*, $\tilde{k}_{on}$, and k_{off}.

for all localizations (see Fig. 1 *d*). However, because of the close docking strand spacing below the achievable localization precision, it is not possible to visually distinguish individual docking strands and localizations overlap within the localization cluster.

Counting single molecules in DNA-PAINT localization clusters

The central question to which lbFCS+ aims to provide an answer is depicted in Fig. 1 *d*. In cases of molecular assemblies such as multimers, the spatial representation of localizations in a DNA-PAINT image often cannot reveal how many docking strands N are contained within a single localization cluster. Furthermore, the spatial representation does not reflect in any sense on the temporal information of imager binding (as given by $\tilde{k}_{on}$ and k_{off}) to the docking strands during image acquisition. Therefore, the quantities N, $\tilde{k}_{on}$, and k_{off} for each localization cluster must be considered unknown. It might further be the case that localization clusters feature distinct values in both N (e.g., because of varying degrees of multimerization or docking strand labeling efficiency) and in $\tilde{k}_{on}$ and k_{off} (e.g., because of the local sample environment affecting the imager accessibility). Hence, an ensemble measurement of $\langle N \rangle$, $\langle \tilde{k}_{on} \rangle$, and $\langle k_{off} \rangle$ would not be able to detect existing heterogeneities in either variable within the sample.

In contrast, the temporal intensity representation of a single localization cluster $I(t)$ (referred to as "intensity trace"; see Fig. 1 *e*) contains the full information of imager binding under appropriately chosen experimental conditions during image acquisition. These conditions include that the reaction of imager-docking strand binding is at equilibrium (e.g., constant imager concentration c and temperature). Sufficiently low excitation intensities have to be employed to reduce possible photophysical artifacts to a minimum such that the binding and blinking kinetics are solely determined by the hybridization rates $\tilde{k}_{on}$ and k_{off}. Explicitly, fluorophore photobleaching of bound imagers needs to be avoided by adjusting laser excitation with respect to k_{off} (32,39). Similarly, the photoinduced loss of docking strands (30,32) (leading to a decrease in N over the measurement time) has to be countered by appropriate measures (low excitation intensities or oxygen scavenger systems). Given that the stated conditions are fulfilled, lbFCS+ is able to find a separate solution N, $\tilde{k}_{on}$, and k_{off} for individual localization clusters solely based on the information contained in their intensity traces.

We want to highlight that the applicability of lbFCS+ is intrinsically limited to targets that give rise to distinct and well-separated localization clusters in a DNA-PAINT image. Potential cellular targets are well-separated target molecule assemblies such as nuclear pore complexes in the nuclear envelope. We have previously published a Python package that allows automated detection and isolation of all localization clusters within a DNA-PAINT image (39,40) (available at https://doi.org/10.5281/zenodo.4792396), constituting the starting point of lbFCS+ analysis.

The analysis approach of lbFCS+

The concept of the lbFCS+ analysis framework is illustrated in Fig. 1 *e* and is applied in parallel to all detected localization clusters in a DNA-PAINT image. In the case of a localization cluster originating from multiple docking strands, the intensity trace $I(t)$ can show intensity fluctuations depending on the number of bound imagers at each time point. First, a step preserving a nonlinear denoising filter (41) is applied to the intensity trace to generate a close-to-steplike behavior according to the number of simultaneously bound imagers (see Fig. S1 *a*). Next, the denoised intensity trace is normalized by the intensity recorded when only a single imager was bound (i.e., to the first intensity level). Hence, after normalization, first-level intensity values have a unitless value of "1" instead of an arbitrary photoelectron count, the second level has a value of "2," and so forth. Further details about the normalization procedure are illustrated in Fig. S1 *b*. Based on the denoised and normalized intensity trace $I_{D+N}(t)$, the occupancy $\hat{\rho}$ and the mean intensity $\langle I_{D+N}(t) \rangle = \hat{I}$ are computed (see *lower left panel* in Fig. 1 *e*). The occupancy $\hat{\rho}$ corresponds to the total time a signal was recorded at the position of the localization cluster divided by the total measurement time, i.e., the fraction the intensity trace was in a fluorescing state.

Analytic expressions for both $\hat{\rho}$ and $\hat{I}$ can be derived under the assumption of equal and independent binding with $\tilde{k}_{on}$ and k_{off} of each imager strand to each of the N docking strands. Then, the probability P_k to find k imager strands simultaneously bound to N docking strands at an arbitrary point in time is given by a binomial distribution:

$$P_k = \binom{N}{k} p^k (1-p)^{N-k} \quad \text{with} \quad p = \frac{1/k_{off}}{1/k_{off} + 1/\tilde{k}_{on}} \tag{1}$$

Intuitively, p corresponds to the probability to find a single docking strand in a fluorescing state, i.e., with an imager bound. The occupancy $\hat{\rho}$ then corresponds to the inverse of the probability P_0 of no imagers bound to the N docking strands:

$$\hat{\rho} = 1 - P_0 = 1 - (1-p)^N \tag{2}$$

The mean intensity $\hat{I}$ is simply given by

$$\hat{I} = \sum_{k=0}^{N} k \binom{N}{k} p^k (1-p)^{N-k} = Np \tag{3}$$

Hence, the expressions for both $\hat{\rho}$ and $\hat{I}$ solely depend on the unknowns N, $\tilde{k}_{on}$, and k_{off}.

Second, the autocorrelation function $G(l)$ of the original localization trace $I(t)$ is computed and $G(l)$ is fitted with a monoexponential decay function yielding the amplitude $\hat{A}$ and the characteristic decay time $\hat{\tau}$ (see *lower right panel* in Fig. 1 *e*). This autocorrelation analysis step is analogous to our previous work lbFCS (32). Again, both $\hat{A}$ and $\hat{\tau}$ have known analytic expressions that solely depend on the unknowns N, $\tilde{k}_{on}$, and k_{off} (32,42):

$$\hat{A} = \frac{1}{N} \frac{k_{off}}{\tilde{k}_{on}} \quad \text{and} \quad \hat{\tau} = \frac{1}{k_{off} + \tilde{k}_{on}} \tag{4}$$

In the final step, the four observables $\hat{\rho}$, $\hat{I}$, $\hat{A}$, and $\hat{\tau}$ derived from the localization trace of each cluster are fed into the defining set of equations and a solution for the unknowns N, $\tilde{k}_{on}$, and k_{off} is found using least-square optimization (see *right panel* in Fig. 1 *e*).

We want to highlight that using this approach, we are only able to find a solution for the effective association rate $\tilde{k}_{on}$, which is dependent on the imager concentration c. However, we can get an "concentration-independent" $k_{on} = \tilde{k}_{on}/c$ inserting the imager concentration c to which the sample was adjusted during sample preparation. Note that the thus-derived "concentration-independent" k_{on} is still prone to pipetting errors, which can only be solved by independent concentration measurements or calibration to a reference sample (see Materials and sample preparation).

We provide a lbFCS+ Python package (43) (available at https://doi.org/10.5281/zenodo.5171076) that automatically computes the solutions for N, $\tilde{k}_{on}$, and k_{off} for all previously detected localization clusters in a DNA-PAINT image.

Materials and sample preparation

This study exclusively features DNA-PAINT experiments on DNA origami as synthetic targets mimicking molecular assemblies of docking strands. Rectangular DNA origami structures were designed using the "Design" module of the Picasso software package (7). Docking strand sequences were "5xCTC" (5′-CTCCTCCTCCTCCTC-3′) and "Pm2*" (5′-TCCTCCTC-3′). Docking strand extended oligos were ordered from IDT (Coralville, IA). The imager of sequence "Pm2" (32) (5′-GAGGAGGA-3′-Cy3b) was ordered from Eurofins (Louisville, KY). The adapter sequences "A20" (5′-AAGAAAGAAAAGAAGAAAAG-3′) and "A20*+5xCTC" (5′-CTTTTCTTCTTTTCTTTCTT_TT_CTCCTCCTC CTCCTC-3′) were ordered from IDT.

The folding reaction mix of each DNA origami design was prepared using 10× folding buffer (100 mM Tris,10 mM EDTA (pH 8.0), 125 mM MgCl2; Ambion, Austin, TX) and the following components: single-stranded M13 bacteriophage DNA scaffold p7249 (0.01 μM; Tilibit, M1-11; Munich, Germany), core staples (0.1 μM; ordered from Eurofins), biotin staples (0.01 μM; ordered from Eurofins), docking strands (1 μM), 1× folding buffer in a total of 50 μL for each folding reaction. Annealing was achieved via cooling the mixture from 80 to 25°C in 3 h in a polymerase chain reaction (PCR) thermocycler. A complete listing of the sequences of the core staples and biotin staples for the rectangular DNA origami design can be found in the supporting material of (7).

Standard DNA-PAINT reagents were ordered and prepared according to (7): buffer A (10 mM Tris-HCl (pH 7.5), 100 mM NaCl; Ambion), buffer B (5 mM Tris-HCl (pH 8.0), 10 mM MgCl2, 1 mM EDTA; Ambion), bovine serum albumin-biotin (A8549; Sigma-Aldrich, St. Louis, MO) diluted at 1 mg/mL in buffer A, and streptavidin (S-888; Thermo Fisher Scientific, Waltham, MA) diluted at 1 mg/mL in buffer A. Eight-well microscopy slides (80826; ibidi, Gräfelfing, Germany) were plasma cleaned for 1 min, then washed 1× with 200 μL buffer A. Each well could be used for an individual experiment, as explained in the following. 200 μL of bovine serum albumin-biotin solution was flushed into the well, incubated for 2 min, removed, and washed 1× with 200 μL buffer A. Next, 200 μL of streptavidin solution was flushed into the well, incubated for 2 min, removed, and washed 1× with 200 μL buffer A and subsequently 1× with 200 μL buffer B. DNA origami solution (diluted 1:200 in buffer B after folding) was flushed into the well, incubated for 5 min, removed, and washed 2× with 200 μL buffer B. Lastly, the desired imager strand concentration was directly adjusted in the well, first adding the required amount of buffer B.

As mentioned in The analysis approach of lbFCS+, pipetting errors directly translate into the obtained result for k_{on}. Therefore, all samples contained a subpopulation of reference origami consisting of $N = 1$ origami carrying a single Pm2* docking strand. Because Pm2* is a subset of our standard docking strand 5xCTC, the same imager Pm2 binds to both Pm2* (reference) and 5xCTC (target) docking strands but at a lower k_{on} (repetitive docking strands such as 5xCTC with multiple imager binding sites increase k_{on} (10,37,39)). Therefore, Pm2 reference localization clusters could be easily separated from 5xCTC clusters by using the occupancy $\hat{\rho}$ during analysis. After separation, resulting variations in k_{on} as obtained from Pm2 reference localization clusters were used for global calibration of the imager concentration.

Imaging

Imaging of DNA origami samples was performed on a custom-built flat-top TIRF (Total Internal Reflection Fluorescence) microscope described in previous studies (31,32,39). All fluorescence microscopy data were recorded with an sCMOS (scientific Complementary Metal–Oxide–Semiconductor) camera (2048 × 2048 pixels, pixel size: 6.5 μm; Andor Zyla 4.2; Belfast, Northern Ireland, UK). The camera was operated with the open-source acquisition software μManager (44) at 2 × 2 binning and cropped to the center 700 × 700 pixel field of view (FOV). The exposure time was set to 400 ms, corresponding to the acquisition duty cycle. The readout rate was 200 MHz, and the dynamic range was set to 16 bits. The nearly homogenous excitation irradiance (31) at the sample was set to ~10 W/cm^2. For detailed imaging parameters specific to the data presented in all main and supplemental figures, refer to Table S1.

RESULTS

Proof-of-principle demonstration of lbFCS+ on DNA origami

As in our previous work (32), we first tested lbFCS+ on DNA origami as synthetic targets that allow precise control of the number of docking strands per target. We designed four DNA origami variants carrying up to six docking strands $N = 1, 2, 4, 6 N = 1, 2, 4, 6$ of the sequence 5xCTC (≡ 5 repetitions of the triplet CTC). Note that here N is an upper bound because of the limited docking strand incorporation efficiency (45), i.e., a sample of $N = 4$ origami will also contain origami carrying only three, two, or even one docking strand(s). We recorded a 30 min DNA-PAINT acquisition at 5 nM imager concentration for each origami variant immobilized on the cover glass of distinct wells of a microscopy slide (see Imaging and Table S1 for detailed imaging conditions of all presented data). After localizing and rendering of the DNA-PAINT images, all localization clusters were automatically detected (see The analysis approach of lbFCS+) and subjected to lbFCS+ analysis.

Fig. 2 *a* shows the obtained counting results for $N = 1$ origami (number of clusters = 1994). The mean of the distribution at $\langle N \rangle = 1.06$ is in close agreement with the expected value of 1 but indicates a slight tendency of overcounting.

The counting results for the DNA-PAINT image of $N = 2$ origami (number of clusters = 2582) in Fig. 2 *b* features a prominent peak at $N \approx 2$ but also a smaller peak at $N \approx 1$ corresponding to origami with one of the two docking strands missing. 82% of all localization clusters lie within $1.5 < N < 3$, which corresponds to an average incorporation efficiency for any of the two docking strands of around 90% (in good agreement with (45)).

The counting results obtained from the $N = 4$ origami image in Fig. 2 *c* (number of clusters = 7232) yielded a distribution with clearly distinguishable peaks located at $N \approx 1$, 2, and 3. Based on the mean of the distribution $\langle N \rangle = 3.35$ (*dashed line*), we estimated a slightly lower incorporation efficiency of around 84% (45). However, we observed a broadening of the distribution toward higher N, hindering a visual distinction of the peak at $N \approx 4$.

This is further confirmed when looking at the counting results derived from the $N = 6$ origami

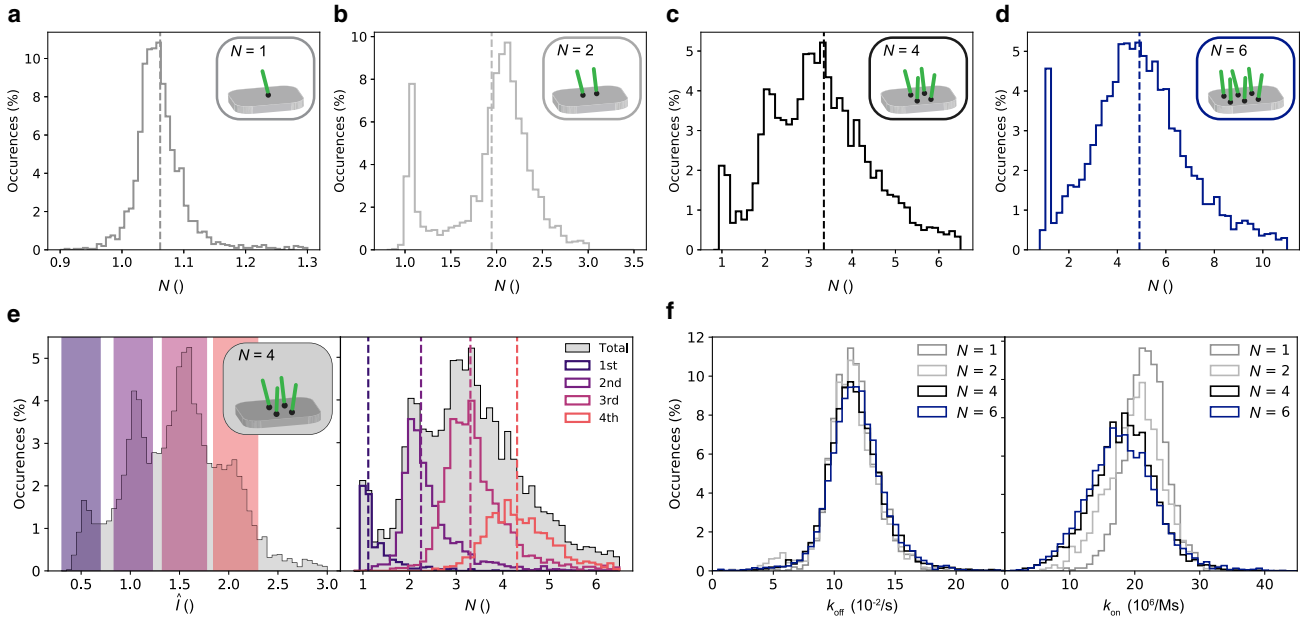

FIGURE 2 Proof-of-principle demonstration on DNA origami. (*a*) Counting results for DNA origami carrying a single docking strand ($N = 1$; number of clusters = 1994) with a mean of $\langle N \rangle = 1.06$ (*dashed line*). (*b*) Same as (*a*) but for DNA origami carrying two docking strands ($N = 2$; number of clusters = 2582; $\langle N \rangle = 1.95$). (*c*) Same as (*a*) but for DNA origami carrying four docking strands ($N = 4$; number of clusters = 7232; $\langle N \rangle = 3.35$). (*d*) Same as (*a*) but for DNA origami carrying six docking strands ($N = 6$; number of clusters = 5038; $\langle N \rangle = 4.91$). (*e*) $\hat{I}$ distribution (*gray*; *left panel*) and *N* distribution (*gray*; *right panel*) for the $N = 4$ origami data set shown in (c). We defined subpopulations by selection of intervals in $\hat{I}$ (*colored intervals*; *left panel*) and plotted their corresponding counting results *N* (*colored solid lines*) and mean values $\langle N \rangle$ (*colored dashed lines*, *right* panel). (*f*) Dissociation rates k_{off} (*left panel*) and association rates k_{on} (*right panel*) obtained via lbFCS+ analysis of all data sets shown in (*a*)–(*d*).

data set (see Fig. 2 *d*). While for $N \geq 5$, it is not possible to visually distinguish incremental copy numbers, the mean of the distribution at $\langle N \rangle = 4.91$ (*dashed line*) still yields a reasonable ensemble average result (corresponding to an incorporation efficiency of around 82%) (45).

Next, we turned back to the $N = 4$ data set to find out whether it is possible to achieve a clear distinction between $N = 3$ and $N = 4$. Remarkably, we found that the distribution of mean intensities $\hat{I}$ obtained from all localization clusters exhibited four peaks, as depicted in the left panel of Fig. 2 *e*. Intuitively, the leftmost peak, i.e., the lowest mean intensity, should correspond to $N = 1$ origami because increasing numbers of docking strands lead to higher values of $\hat{I}$ because of the increasing probability of simultaneous binding of multiple imagers (see Eq. 3). We confirmed this by selecting localization clusters lying within the colored intervals in $\hat{I}$ and by comparing the corresponding subpopulations in *N* to the overall obtained distribution (Fig. 2 *e*, *left* and *right*, respectively). This selection in $\hat{I}$ allowed us to obtain mean counting results for the subpopulations that are close to the expected values of $N = 1$, 2, 3, and 4 (*colored dashed lines*). The visual inspection of exemplary intensity traces from the selected intervals in $\hat{I}$ confirms the applicability of this approach (see Fig. S2). Again, we observed a slight overcounting that is more prominent for increasing *N*.

After inspection of the counting results, we turned our attention to the imager hybridization rates obtained via lbFCS+ analysis of the same four data sets as in Fig. 2, *a*–*d*. Fig. 2 *f* shows the corresponding k_{off} distributions (*left*) and k_{on} distributions (note that lbFCS+ yields $\tilde{k}_{on}$, from which $k_{on} = \tilde{k}_{on}/c$ was calculated using the absolute imager concentration; see Brief recap of SMLM and DNA-PAINT binding dynamics). Overall, k_{off} shows very good agreement for all four data sets independent of the number of docking strands per origami with a relative width of standard deviation $\mathrm{STD}(k_{off})/\langle k_{off} \rangle \approx 18\%$.

In k_{on}, however, we observed broader distributions compared to k_{off} with relative widths $\mathrm{STD}(k_{on})/\langle k_{on} \rangle$ increasing from 14% for $N = 1$ to 30% for $N = 6$. Additionally, we observed a slight but systematic decrease with increasing numbers of docking strands with $\langle k_{on} \rangle$ decreasing from 22×10^6 1/Ms for $N = 1$ to 18×10^6 1/Ms for $N = 6$. As described in Materials and sample preparation, reference origami allowed for a calibration of the imager concentrations to minimize pipetting errors affecting k_{on} (see Fig. S3 for the calibration results of the $N = 1$, 2, 4, 6 data sets shown in Fig. 2, *a*–*d*).

Both the experimentally observed upper limit in distinguishing copy numbers of $N \geq 4$ and the apparent

dependence of k_{on} on N led us to further assess the applicable working range of lbFCS+.

Assessing the working range of lbFCS+

To investigate the applicable working range of lbFCS+ and possible systematic artifacts, it was obligatory to perform the analysis on a data set of known ground truth. Therefore, we computationally combined arbitrary localization clusters from the $N = 1$ data set (see Fig. 2 *a*) into clusters of user-defined $N_{in} = k \times (N = 1)$, a concept we already applied in an earlier study (32). This "regrouping" is equivalent to the computational addition of intensity traces $I(t)$ of the individual clusters. To exclude varying intensity levels between the original clusters (e.g., caused by speckles in the illumination profile), the intensity traces $I(t)$ were normalized before addition (see Fig. S1). We want to highlight that this procedure completely preserved the experimental intensity noise distribution.

Fig. 3 *a* shows the counting results obtained from computationally regrouped clusters consisting of up to eight experimental $N = 1$ clusters (i.e., $N_{in} = k \times (N = 1)$ up to $k = 8$). Overall, the counting results N agree very well with the expected N_{in}. Again, we observed a slight systematic offset of the resulting means $\langle N \rangle$ (*colored dashed lines*) toward higher N. Although this effect seemed to increase with N_{in} in absolute terms, the relative offsets $((\langle N \rangle - N_{in})/N_{in}$ remained constant at ~6% (compare to Fig. 2 *a*). We believe that this systematic offset might be due to unaccounted sampling effects from discretizing the recorded fluorescence signals into single frames. Another possibility could be the minimal net gradient parameter determining the intensity threshold for localization detection (see The analysis approach of lbFCS+ and (40)). However, for both resolving integers from one to four docking strands and for counting of up to 10 docking strands, a systematic overcounting offset of 6% is negligible. Similar to the experimental results, the width of the N distributions broadened with increasing N_{in} (compare to Fig. 2, *a*–*e*).

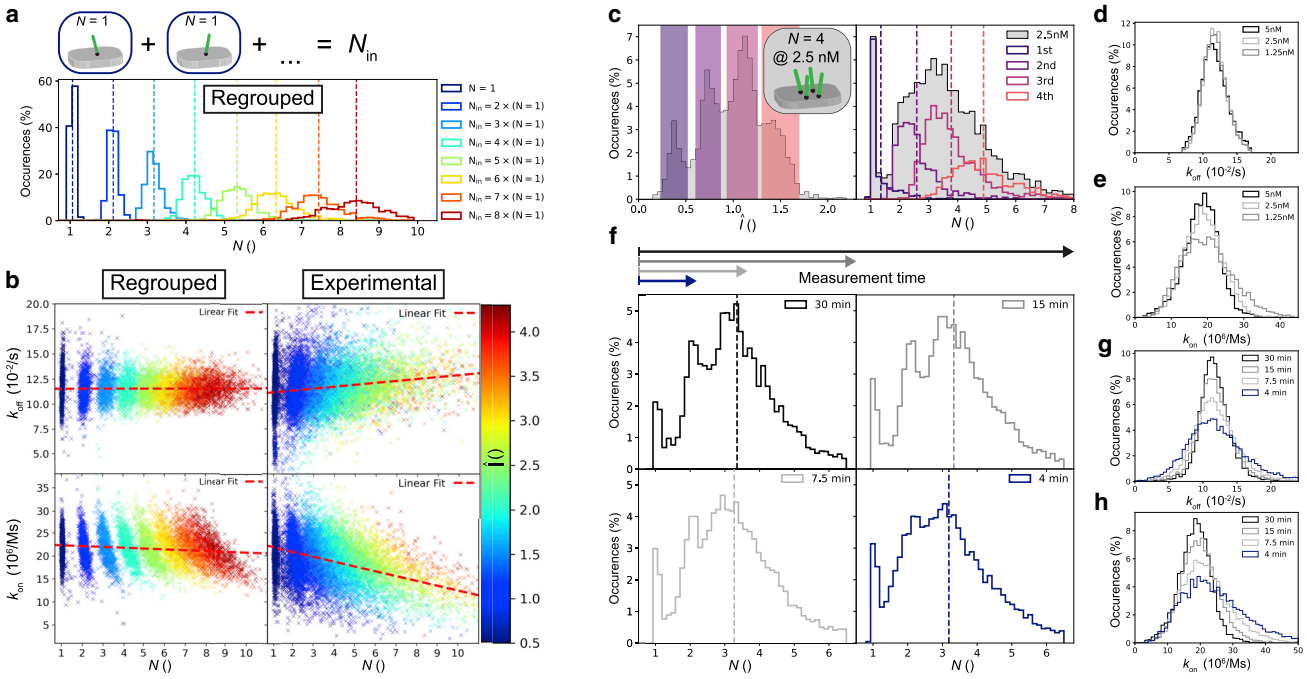

FIGURE 3 Assessing the working range of lbFCS+. Localization clusters from the $N = 1$ data set (see Fig. 2 *a*) were selected at random and subsequently computationally combined into clusters of user-defined $N_{in} = k \times (N = 1)$ and subjected to lbFCS+ analysis (number of clusters = 1000 for each N_{in}). (*a*) Counting results N obtained from computationally combined clusters consisting of up to eight experimental $N = 1$ clusters (i.e., $N_{in} = k \times (N = 1)$ up to $k = 8$) and their corresponding means $\langle N \rangle$ (*dashed lines*). (*b*) Scatter plot k_{off} vs. N (*upper panels*) and scatter plot k_{on} vs. N (*lower panels*) for all computationally combined clusters (*left* panels) shown in (*a*) and for all experimental clusters from $N = 1$, 2, 4, 6 origami (*right panels*) shown in Fig. 2, *a*–*d*. Each cluster was color coded according to its mean intensity $\hat{I}$ (which is linearly proportional to N; see Eq. 3). The red dashed lines indicate the optimal linear fits over all data points in each panel. (*c*) Analysis analogous to Fig. 2 *e* for DNA origami containing four docking strands ($N = 4$) but measured at a reduced imager concentration of 2.5 nM (number of clusters = 3697). (*d*) Dissociation rates k_{off} obtained via lbFCS+ analysis for DNA origami containing four docking strands ($N = 4$) measured at varying imager concentrations (number of clusters = 5834 for 1.25 nM). (*e*) Association rates k_{on} for the same data sets as in (*d*). (*f*) Counting results for the $N = 4$ origami data set shown in Fig. 2 *c* for varying measurement times. The original data set (30 min measurement time) was reduced to the first 15, 7.5, and 4 min, respectively, before analysis. The dashed lines indicate the mean $\langle N \rangle$ of each distribution. (*g*) Dissociation rates k_{off} obtained via lbFCS+ analysis for the data shown in (*g*). (*h*) Association rates k_{off} obtained via lbFCS+ analysis for the data shown in (*g*).

The relative width of each distribution defined as STD(N)/$\langle N \rangle$ increased proportional to $\sqrt{N_{in}}$, starting with a value of 4% for $N = 1$. This broadening behavior is in line with the experimental N results displayed in Fig. 2, *a–d*. However, from our regrouping analysis, we would expect that it should be possible to clearly distinguish the peaks between $N = 3$ and $N = 4$, which is not the case for DNA origami (see Fig. 2 *c*). This indicates an additional source of uncertainty of lbFCS+ counting toward higher N.

Next, we focused on the hybridization rates obtained from the regrouped data sets. The upper left panel of Fig. 3 *b* shows a scatter plot of the obtained k_{off} vs. N result for all localization clusters from the eight regrouped data sets. Each cluster was color coded using its respective mean intensity value $\hat{I}$ (which is linearly proportional to N; see Eq. 3). Contrarily to the broadening in N, we observed a narrowing of the k_{off} distributions for increasing N_{in}. Both the shape of the distributions with respect to k_{off} and N as well as the negligible slope of a linear fit of all data points (*red dashed line*) indicated that the solutions for k_{off} and N are largely decoupled.

Similarly, the lower left panel of Fig. 3 *b* shows the analogous scatter plot for k_{on} vs. N. Here, the linear fit over all clusters exhibited a minor but negligible decrease in k_{on} for increasing N with respect to experimental measurement errors (see description of Fig. 2 *f* in Proof-of-principle demonstration of lbFCS+ on DNA origami). Furthermore, we observed a hyperbolic shape of the k_{on} vs. N distributions for increasing N_{in}. This is due to the fact that three of the four observables ($\hat{\rho}$, $\hat{I}$, and $\hat{A}$) used as input to the final set of equations (see Fig. 1 *e*, *right*) are in first-order approximation proportional or indirectly proportional to the product $N\tilde{k}_{on}$ (see Eq. 2, 3, and 4). Additionally, the observable $\hat{\rho}$ only contains valuable information for fluorescence traces featuring interruptions, thereby constituting an upper operational limit of lbFCS+ at a given imager concentration. For increasing N, almost uninterrupted intensity traces lead to saturation of $\hat{\rho}$ (e.g., $\hat{\rho} \sim 99\%$ for $N_{in} = 8$) and as such to a loss of information for the defining set of equations. For this reason, lbFCS+ is designed for application to targets containing low copy numbers of docking strands $N \leq 10$ (depending on the used imager concentration and k_{on}). To experimentally assess its upper limit, we imaged and analyzed origami containing up to 12 docking strands. As expected from Fig. 3 *a*, we were not able to resolve between integers anymore but observed a reasonable counting result distribution with a mean of $\langle N \rangle = 9.34$ when imaged at a concentration of 2.5 nM (see Fig. S4).

To compare the findings obtained from computational regrouping to the experimental data, we depicted the combined results from $N = 1, 2, 4, 6$ origami (see Fig. 2, *a–d*) in an analogous k_{off} vs. N scatter plot in the upper right panel of Fig. 3 *b*. In contrast to the computationally combined clusters, linear fitting over all experimental clusters (*red dashed line*) indicated an increase in k_{off} with N. On the other hand, the experimentally obtained k_{on} vs. N scatter plot in the lower right panel of Fig. 3 *b* similarly yields increasingly hyperbolic distributions as observed for the regrouped clusters. Linear fitting of all data points (*red dashed line*) showed a clear decrease in k_{on} with increasing N, as already observed in Fig. 2 *f*. This decrease in k_{on} with increasing N is significantly larger compared to the regrouped data sets (see *lower left panel*).

The observations in both k_{on} and k_{off} indicated that intensity traces recorded from origami containing multiple docking strands are not exactly equal to the simple addition of the individual single docking strand signals. We suspected that the docking strand position on the DNA origami could lead to local changes in k_{on} and k_{off}, thereby possibly giving rise to a measurement bias for higher N. Remarkably, when performing four control experiments, each time only with one of the four docking strands of the $N = 4$ origami incorporated, we could not observe any position dependence either in k_{on} or in k_{off} (see Fig. S5). We hypothesize that cooperative binding due to the spatial proximity of the docking strands could be a possible explanation for this behavior. However, over the applicable range of $N \lesssim 4–8$, this does not affect the ability of lbFCS+ to obtain correct counting results and only causes minor deviations in the measured hybridization rates (≤ 2 and $\leq 20\%$ in k_{off} and k_{on}, respectively).

As a next step, we assessed the lower limit of the applicable working range by measuring $N = 4$ origami at reduced imager concentrations. Analogous to Fig. 2 *e*, it was still possible to clearly distinguish subpopulations in $\hat{I}$ to identify the corresponding result in N but at a reduced imager concentration of 2.5 nM (see Fig. 3 *c*). It was even possible to repeat the same analysis for a sample imaged at an imager concentration of 1.25 nM (see Fig. S6). The shapes of the N distributions are in close agreement with the results obtained from the computational combination of experimental $N = 1$ clusters measured at a concentration of 1.25 nM to clusters of defined $N_{in} = k \times (N = 1)$ as presented in Fig. S7 (analogous to Fig. 3, *a* and *b*).

Surprisingly, imaging $N = 4$ origami at lower imager concentrations had no significant effect on the resulting k_{off}-values as shown in Fig. 3 *d*. However, we observed a broadening in k_{on} with decreasing imager concentrations as expected from the broadening in N (see Fig. 3 *e*).

Finally, we investigated the effects of the measurement time on lbFCS+ analysis (i.e., the image

acquisition time). We therefore reduced the original $N = 4$ data set (30 min measurement time) to the first 15, 7.5, and 4 min before analysis. Remarkably, it was only possible to observe significant changes in the resulting N distribution at measurement times $\lesssim$8 min (see Fig. 3 *f*). A measurement time of 4 min would correspond to an expectation value of only ~13 imager binding events per single docking strand. We observed a broadening in both k_{off} and k_{on} for reduced measurement times as apparent from Fig. 3, *g* and *h*, respectively. Finally, our optimization of the required measurement times allowed us to image 18 FOVs containing a total of ~50,000 origami in ~3 h of total measurement time, still yielding robust quantitative results (see Fig. S8).

Distinction of nanoscopic DNA assemblies via binding dynamics

Driven by the high accuracy of lbFCS+ to determine hybridization rates, we hypothesized that it might be possible to distinguish DNA constructs via detection of slight changes in the position-dependent imager-docking strand binding dynamics.

Besides the direct incorporation of 5xCTC docking strands as used in the preceding experiments, we designed DNA origami carrying a single 20 base "adapter" docking strand of sequence A20 (see Materials and sample preparation for exact sequences). Addition of oligos carrying both the complementary adapter region and the docking strand sequence (A20*+5xCTC, referred to as "linker strand") allowed us to permanently install the docking strand further away from the origami surface via the double-stranded link A20 + A20* (~10 nm at full elongation), as depicted in Fig. 4 *a*. We distinguished between the "Direct" configuration (5xCTC incorporated; *gray box*) and the "Link" configuration (5xCTC on top of the double-stranded A20 linker; *orange box*). We want to highlight that both configurations are not rigid but experience rotational freedom introduced by single-stranded TT spacers (*black dots*; one for Direct and two for Link, respectively).

We subsequently imaged three samples containing 1) only Direct origami, 2) only Link origami, or 3) a mixture of both configurations. lbFCS+ analysis yielded the expected number of docking strands $N = 1$ (see Fig. 4 *b*) in all cases, and we could not observe any alteration of k_{off} between the different configurations (see Fig. 4 *c*). In contrast, we observed an increased k_{on} for the Link configuration compared to the Direct configuration (see Fig. 4 *d*). We suppose that both the increased mobility of the docking strand and larger distance from the origami surface promote a higher chance of imager binding for the Link configuration. This shift was large enough to clearly identify the Link or Direct origami in the bimodal k_{on} distribution of the sample containing both configurations (Mix).

Following the same reasoning, we designed DNA origami similar to the Link assembly (see Fig. 4 *a*) but now providing a second possible binding site for the A20 adapter (referred to as "2xLink"; see Fig. 4 *e*). Because of the stochastic nature of linker strand binding, this origami configuration can be observed in one of three possible states. The first two states consist of a single linker strand (i.e., $N = 1$) bound to the 2xLink origami at either the bottom or the top (*blue box* in Fig. 4 *e*). The third state corresponds to both A20 sites (i.e., $N = 2$) being occupied by a linker strand (*dark red box* in Fig. 4 *e*). Because the ratio of origami in an $N = 1$ or $N = 2$ configuration should be manipulable via variation of linker strand concentrations, we imaged four samples of 2xLink origami that were previously incubated for 3 min at 100, 40, 5, and 2 nM linker strand concentrations.

Fig. 4 *f* shows the total N distribution obtained from lbFCS+ analysis of the four data sets (*gray*), confirming the expected counting result of either $N = 1$ or $N = 2$. Although for a 100 nM linker strand concentration, ~80% of all origami had bound two linkers, at 2 nM it was only ~60%, validating the concentration dependence during incubation on the probability of 2xLink origami to be found in an $N = 1$ or $N = 2$ state (see Fig. S9).

Again, we were interested in potential variations in the measured hybridization rates depending on the state of each 2xLink origami. For this reason, we isolated the $N = 1$ and $N = 2$ configurations by separating localization clusters that yielded either $N < 1.2$ (*blue*) or $N > 1.6$ (*dark red*), respectively (see Fig. 4 *f*). Already, the total k_{off} distribution of all 2xLink origami (*gray*) presented in Fig. 4 *g* revealed two subpopulations located at $k_{off} \approx 7 \times 10^{-2}$ 1/s and $k_{off} \approx 11 \times 10^{-2}$ 1/s. These two subpopulations became especially prominent when looking at only $N = 1$ localization clusters (*blue*), confirming the existence of a top and a bottom state of $N = 1$ origami that give rise to a distinct k_{off}. In contrast, the $N = 2$ clusters yielded a homogeneous k_{off} distribution with a median (*dark red arrow*) nearly identical to the median of previous Link origami (*orange arrow*, obtained from *orange distribution* shown in Fig. 4 *c*).

Inspection of the k_{on} results yielded a similar behavior, as depicted in Fig. 4 *h*. While the total k_{on} distribution showed a somewhat broadened shape (*gray*), selection of $N = 1$ origami clearly revealed two subpopulations located at $k_{on} \approx 17 \times 10^6$ M/s and $k_{on} \approx 31 \times 10^6$ M/s. This suggested that for $N = 1$ origami, the top and bottom states also give rise to a different k_{on}. The k_{on}-values obtained from $N = 2$ origami resulted in a

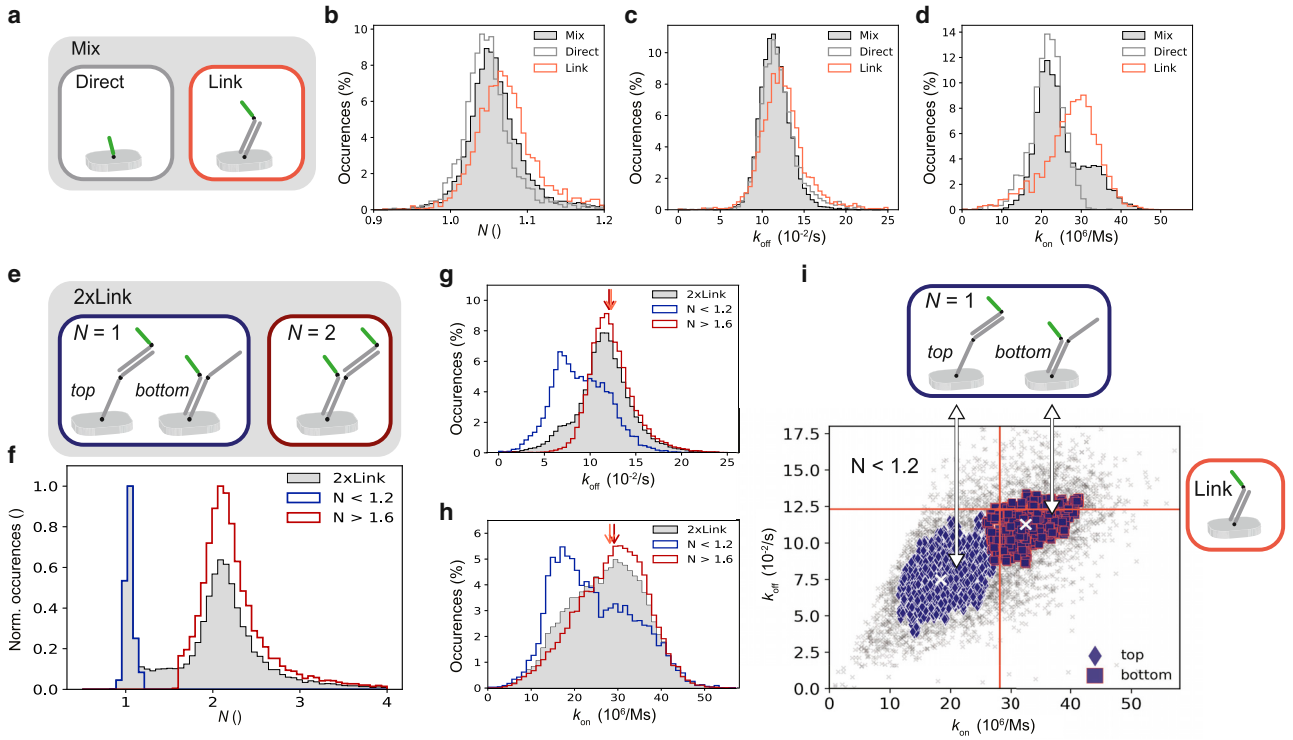

FIGURE 4 Distinction of nanoscopic DNA assemblies via binding dynamics. (*a*) Schematic of the direct incorporation of 5xCTC docking strands into DNA origami ("Direct"; *dark gray box*) and permanent attachment of 5xCTC docking strands via a "linker strand" (A20*+5xCTC) after folding ("Link"; *orange box*). Black dots indicate single-stranded TT spacers. We imaged three samples containing 1) only Direct origami, 2) only Link origami, or 3) a mixture of both configurations ("Mix"; *solid gray box*). (*b*) lbFCS+ counting results as obtained from the Direct origami, the Link origami, and the mixed sample as illustrated in (*a*). Direct sample contained number of clusters = 2088; Link: number of clusters = 2780; Mix: number of clusters = 9136. (*c*) Dissociation rate k_{off} as obtained from the same data as shown in (*b*). (*d*) Association rate k_{on} as obtained from the same data as shown in (*b*). (*e*) DNA origami design featuring 2x linker binding sites (referred to as "2xLink"). After incubation with linker strands, 2xLink origami can be in three possible states (schematically depicted). The first two states consist of a single linker strand (i.e., $N = 1$) bound to the 2xLink origami at either the bottom or the top position (*blue box*). The third state corresponds to both A20 sites being occupied by a linker strand (i.e., $N = 2$; *dark red box*). (*f*) Total *N* distribution obtained from imaging four distinct samples of 2xLink origami, which were incubated for 3 min at 100, 40, 5, or 2 nM linker strand concentrations (Fig. S9 shows separate results for each sample). For further analysis, we split the total distribution into clusters yielding either $N < 1.2$ (*blue*) or $N > 1.6$ (*dark red*). Total number of 2xLink origami localization clusters from four data sets = 27,348; $N < 1.2$: number of clusters = 6159; $N > 1.6$: number of clusters = 19,192. (*g*) Dissociation rate k_{off} as obtained from the same data as shown in (*f*). The dark red arrow indicates the median of the $N > 1.6$ subpopulation, and the orange arrow indicates the median of the Link origami shown in (*c*). (*h*) Results analogous to (*g*) but for the association rate k_{on}. (*i*) Scatter plot of k_{off} vs. k_{on} for all 2xLink origami yielding $N < 1.2$; see (*f*). Hierarchical density-based clustering (46) (used parameters: metric = `l2,' min_cluster_size = 500, min_samples = 8) of the data yielded two groups. The median of each group is marked by a white cross, and the corresponding median as obtained from Link origami shown in (*c*) and (*d*) is indicated by the orange lines. We assigned the bottom $N = 1$ state of the 2xLink origami to the upper right group (*dark blue squares*) because of 1) the proximity of its median to the median of the Link origami and 2) its resemblance in design to the Link origami (compare *orange box* in *a* with blue box in *e*). Vice versa, we assigned the top $N = 1$ state of the 2xLink origami to the lower left group (*dark-blue diamonds*). All $N < 1.2$ origami contained number of clusters = 6159; top: number of clusters = 2630; bottom: number of clusters = 981.

broad distribution with a skew toward lower k_{on}-values. However, its median (*dark red arrow*) was again close to the median in k_{on} as obtained for the Link origami (*orange arrow*, obtained from *orange distribution* shown in Fig. 4 *d*).

In conclusion, this suggests that the signal from $N = 2$ origami is actually a superposition of heterogeneous signals due to the distinct binding dynamics of the top and bottom $N = 1$ states. Strictly speaking, here $N = 2$ origami, hence violating our assumption of equal and independent binding rates used in the derivation of The analysis approach of lbFCS+. The coincidence of the $N = 2$ peak (*dark red*) with the right peaks of the two possible $N = 1$ configurations (*blue*) indicates that in the case of heterogeneous rates, lbFCS+ analysis is dominated by the larger value in both k_{off} and k_{on} (see Fig. 4, *g* and *h*, respectively). Regardless of heterogeneous rates, lbFCS+ analysis still yielded the correct counting results (compare Fig. 4 *f*).

Finally, we aimed to exploit the heterogeneous binding kinetics to identify the (otherwise indistinguishable) top/bottom states within the $N = 1$ subpopulation.

Indeed, hierarchical density-based clustering (46) allowed us to classify two distinct states in the scatter plot of k_{off} vs. k_{on} over all $N = 1$ localization clusters (see Fig. 4 *i*). Intuitively, the bottom $N = 1$ state of the 2xLink origami should be close to the Link configuration depicted in Fig. 4 *a*. Comparison of the median k_{off} and k_{on} of each class (*white crosses*) with the median k_{off} and k_{on} as obtained for the Link origami *(orange lines*, obtained from Fig. 4, *b* and *d*) hence allowed us to associate the top right class (*square*) with the bottom $N = 1$ state and the top left class with the top $N = 1$ state (*diamonds*). We classified almost three times as many origami in a top state (number of clusters = 2630) as in a bottom state (number of clusters = 981), suggesting a lower binding probability of linker strands to the bottom position. Interestingly, we observed a significantly lower k_{off} (i.e., a longer binding duration) and a lower k_{on} for docking strands placed at the top position when compared to the bottom position.

DISCUSSION

In summary, lbFCS+ is, to our knowledge, the first method capable of extracting both absolute molecular copy numbers and DNA hybridization rates of individual DNA-PAINT localization clusters within a single DNA-PAINT image. Based on only minimal experimental requirements and theoretical assumptions, it thus provides a potential solution to the long prevailing problem of "molecular counting" in SMLM without the need of any initial calibration or modeling (11,25,33).

In proof-of-principle experiments on DNA origami, we demonstrated that lbFCS+ yields truthful docking strand copy numbers *N* and dissociation and association rates k_{off} and k_{on} of the underlying imager-docking strand binding reaction from DNA-PAINT data sets acquired at moderate imager concentrations ($\leq$5 nM) and measurement times ($\leq$30 min). Our assessment of the working range indicated that lbFCS+ is suited for an application to localization clusters containing up to 10 docking strands. However, because of the broadening of the counting result distributions with higher *N*, it is only possible to resolve between integers for up to four docking strands. This might become a useful feature for studying the composition of up to tetrameric molecular complexes in the future. The high accuracy of lbFCS+ to determine hybridization rates allowed us to measure small differences in imager binding dynamics to docking strands of same sequence but placed at different positions of nanoscopic DNA assemblies. Finally, this enabled us to resolve heterogeneous binding dynamics between individual DNA-PAINT clusters, allowing for the distinction of stochastically generated and a priori indistinguishable DNA assemblies.

Although this work was limited to planar samples imaged in TIRF configuration, we would like to note that lbFCS+ is potentially also applicable to three-dimensional (3D) data sets. Usually, 3D DNA-PAINT image acquisition requires a confined illumination scheme (e.g., highly inclined and laminated optical sheet or spinning disk confocal microscopy) to suppress the fluorescent background from the imaging solution. However, 3D DNA-PAINT imaging possibly suffers from a decreased signal/noise ratio due to out-of-focus fluorescence. In addition, 3D-SMLM approaches commonly result in a lower axial resolution compared with the achievable lateral resolution, which requires carefully adjusting the analyzed cluster volumes (47). Both effects can negatively affect the working range of lbFCS+ such that the actual compatibility of lbFCS+ with 3D DNA-PAINT remains to be carefully evaluated. Recently, fluorogenic imagers have been proposed to greatly reduce background fluorescence in 3D DNA-PAINT imaging (48), which might be beneficial along this direction.

Because lbFCS+ does not rely on any ensemble averaging, it would be ideally suited for the study of heterogeneous samples as expected in, e.g., cellular environments. Heterogeneities might emerge from diffusional barriers because of compartmentalization or steric hindrance in densely packed molecular environments. lbFCS+ could hence map the accessibility of imagers to different cellular parts (decoupled from the molecular copy numbers), which could be of general interest for the interpretation of DNA-PAINT images. Because of its accuracy in the determination of low molecular copy numbers especially, studies aiming for the distinction of monomers, dimers, or tetramers are a feasible first step. We reason that high target molecule densities (11), pronounced unspecific binding of imager strands (37,49), and the optical sectioning capabilities of the used microscope will be major challenges when applying lbFCS+ to cellular targets. We want to highlight that DNA-PAINT (and hence lbFCS+) is generally not designed for living cells but requires fixed specimens. Finally, lbFCS+ requires the presence of well-separated localization clusters in the DNA-PAINT image and cannot, as such, be readily transferred to an analysis of, e.g., continuous objects.

We demonstrated that lbFCS+ is capable of detecting or distinguishing small differences in imager-docking strand binding dynamics in nanoscopic volumes containing low numbers of molecules requiring only moderate measurement times. Hence, lbFCS+ provides a highly parallelized and easy-to-implement readout for potential on-chip biosensing applications. Especially interesting are applications requiring a direct detection of molecules in low-concentration regimes without amplification steps (50,51). Additionally, our

study of varying DNA assemblies already suggests that lbFCS+ might readily serve as a readout to determine the state of logic gates (e.g., hairpins) in DNA-based logical circuits (52,53). However, we want to highlight that lbFCS+ is in principle not limited to the study of DNA hybridization reactions but can applied to any reversible binding reaction of fluorescently labeled ligands to immobilized receptors.

In conclusion, we believe that lbFCS+ provides a powerful tool with promising applications beyond its initial purpose of advancing quantitative DNA-PAINT imaging.

SUPPLEMENTAL INFORMATION

Supplemental information can be found online at https://doi.org/10.1016/j.bpr.2021.100032.

AUTHOR CONTRIBUTIONS

J.S., F.S., and P.S. conceived the study. J.S. and F.S. designed and performed experiments. J.S. and F.S. designed and performed data analysis. F.S. wrote the analysis code. J.S., F.S., and P.S. wrote the manuscript. P.S. supervised the study. The co-first authorship order was determined via the best of three rounds in rock-paper-scissors at the start of the first authors' PhD life. Both J.S. and F.S. contributed equally. All authors discussed and interpreted results and revised the manuscript.

DECLARATION OF INTERESTS

The authors declare no competing interests.

ACKNOWLEDGMENTS

We thank Jan-Hagen Krohn for the implementation of the Chung-Kennedy filter in Python and for design of the A20 adapter sequence. Further, we thank Sigrid Bauer and Sebastian Strauss for experimental support.

J.S. and F.S. acknowledge support from Graduate School of Quantitative Bioscience Munich. All authors acknowledge support from the Center for Nano Science. This work has been supported in part by the German Research Foundation through SFB1032 (projects A11 and A09 to R.J. and P.S.) and the Max Planck Society (R.J. and P.S.).

REFERENCES

1. Hell, S. W., and J. Wichmann. 1994. Breaking the diffraction resolution limit by stimulated emission: stimulated-emission-depletion fluorescence microscopy. *Opt. Lett.* 19:780–782.
2. Klar, T. A., S. Jakobs, …, S. W. Hell. 2000. Fluorescence microscopy with diffraction resolution barrier broken by stimulated emission. *Proc. Natl. Acad. Sci. USA.* 97:8206–8210.
3. Betzig, E., G. H. Patterson, …, H. F. Hess. 2006. Imaging intracellular fluorescent proteins at nanometer resolution. *Science.* 313:1642–1645.
4. Rust, M. J., M. Bates, and X. Zhuang. 2006. Sub-diffraction-limit imaging by stochastic optical reconstruction microscopy (STORM). *Nat. Methods.* 3:793–795.
5. Sharonov, A., and R. M. Hochstrasser. 2006. Wide-field subdiffraction imaging by accumulated binding of diffusing probes. *Proc. Natl. Acad. Sci. USA.* 103:18911–18916.
6. Jungmann, R., C. Steinhauer, …, F. C. Simmel. 2010. Single-molecule kinetics and super-resolution microscopy by fluorescence imaging of transient binding on DNA origami. *Nano Lett.* 10:4756–4761.
7. Schnitzbauer, J., M. T. Strauss, …, R. Jungmann. 2017. Super-resolution microscopy with DNA-PAINT. *Nat. Protoc.* 12:1198–1228.
8. Thompson, R. E., D. R. Larson, and W. W. Webb. 2002. Precise nanometer localization analysis for individual fluorescent probes. *Biophys. J.* 82:2775–2783.
9. Deschout, H., F. Cella Zanacchi, …, K. Braeckmans. 2014. Precisely and accurately localizing single emitters in fluorescence microscopy. *Nat. Methods.* 11:253–266.
10. Strauss, S., and R. Jungmann. 2020. Up to 100-fold speed-up and multiplexing in optimized DNA-PAINT. *Nat. Methods.* 17:789–791.
11. Baddeley, D., and J. Bewersdorf. 2018. Biological insight from super-resolution microscopy: what we can learn from localization-based images. *Annu. Rev. Biochem.* 87:965–989.
12. Annibale, P., S. Vanni, …, A. Radenovic. 2011. Quantitative photo activated localization microscopy: unraveling the effects of photoblinking. *PLoS One.* 6:e22678.
13. Annibale, P., S. Vanni, …, A. Radenovic. 2011. Identification of clustering artifacts in photoactivated localization microscopy. *Nat. Methods.* 8:527–528.
14. Coltharp, C., R. P. Kessler, and J. Xiao. 2012. Accurate construction of photoactivated localization microscopy (PALM) images for quantitative measurements. *PLoS One.* 7:e51725.
15. Lee, S. H., J. Y. Shin, …, C. Bustamante. 2012. Counting single photoactivatable fluorescent molecules by photoactivated localization microscopy (PALM). *Proc. Natl. Acad. Sci. USA.* 109:17436–17441.
16. Puchner, E. M., J. M. Walter, …, W. A. Lim. 2013. Counting molecules in single organelles with superresolution microscopy allows tracking of the endosome maturation trajectory. *Proc. Natl. Acad. Sci. USA.* 110:16015–16020.
17. Nan, X., E. A. Collisson, …, S. Chu. 2013. Single-molecule super-resolution imaging allows quantitative analysis of RAF multimer formation and signaling. *Proc. Natl. Acad. Sci. USA.* 110:18519–18524.
18. Ehmann, N., S. van de Linde, …, R. J. Kittel. 2014. Quantitative super-resolution imaging of Bruchpilot distinguishes active zone states. *Nat. Commun.* 5:4650.
19. Rollins, G. C., J. Y. Shin, …, S. Pressé. 2015. Stochastic approach to the molecular counting problem in superresolution microscopy. *Proc. Natl. Acad. Sci. USA.* 112:E110–E118.
20. Fricke, F., J. Beaudouin, …, M. Heilemann. 2015. One, two or three? Probing the stoichiometry of membrane proteins by single-molecule localization microscopy. *Sci. Rep.* 5:14072.
21. Ricci, M. A., C. Manzo, …, M. P. Cosma. 2015. Chromatin fibers are formed by heterogeneous groups of nucleosomes in vivo. *Cell.* 160:1145–1158.
22. Hummer, G., F. Fricke, and M. Heilemann. 2016. Model-independent counting of molecules in single-molecule localization microscopy. *Mol. Biol. Cell.* 27:3637–3644.
23. Laplante, C., F. Huang, …, T. D. Pollard. 2016. Molecular organization of cytokinesis nodes and contractile rings by super-resolution fluorescence microscopy of live fission yeast. *Proc. Natl. Acad. Sci. USA.* 113:E5876–E5885.

24. Nino, D., N. Rafiei, …, J. N. Milstein. 2017. Molecular counting with localization microscopy: a Bayesian estimate based on fluorophore statistics. *Biophys. J.* 112:1777–1785.
25. Nicovich, P. R., D. M. Owen, and K. Gaus. 2017. Turning single-molecule localization microscopy into a quantitative bioanalytical tool. *Nat. Protoc.* 12:453–460.
26. Golfetto, O., D. L. Wakefield, …, T. Jovanović-Talisman. 2018. A platform to enhance quantitative single molecule localization microscopy. *J. Am. Chem. Soc.* 140:12785–12797.
27. Hess, S. T., T. P. K. Girirajan, and M. D. Mason. 2006. Ultra-high resolution imaging by fluorescence photoactivation localization microscopy. *Biophys. J.* 91:4258–4272.
28. Heilemann, M., S. van de Linde, …, M. Sauer. 2008. Subdiffraction-resolution fluorescence imaging with conventional fluorescent probes. *Angew. Chem. Int. Ed. Engl.* 47:6172–6176.
29. Demchenko, A. P. 2020. Photobleaching of organic fluorophores: quantitative characterization, mechanisms, protection. *Methods Appl. Fluoresc.* 8:022001.
30. Blumhardt, P., J. Stein, …, P. Schwille. 2018. Photo-induced depletion of binding sites in DNA-PAINT microscopy. *Molecules.* 23:3165.
31. Stehr, F., J. Stein, …, R. Jungmann. 2019. Flat-top TIRF illumination boosts DNA-PAINT imaging and quantification. *Nat. Commun.* 10:1268.
32. Stein, J., F. Stehr, …, P. Schwille. 2019. Toward absolute molecular numbers in DNA-PAINT. *Nano Lett.* 19:8182–8190.
33. Lelek, M., M. T. Gyparaki, …, C. Zimmer. 2021. Single-molecule localization microscopy. *Nat. Rev. Methods Prim.* 1:39.
34. Jungmann, R., M. S. Avendaño, …, P. Yin. 2016. Quantitative super-resolution imaging with qPAINT. *Nat. Methods.* 13:439–442.
35. Schickinger, M., M. Zacharias, and H. Dietz. 2018. Tethered multi-fluorophore motion reveals equilibrium transition kinetics of single DNA double helices. *Proc. Natl. Acad. Sci. USA.* 115:E7512–E7521.
36. Schueder, F., J. Stein, …, R. Jungmann. 2019. An order of magnitude faster DNA-PAINT imaging by optimized sequence design and buffer conditions. *Nat. Methods.* 16:1101–1104.
37. Clowsley, A. H., W. T. Kaufhold, …, C. Soeller. 2021. Repeat DNA-PAINT suppresses background and non-specific signals in optical nanoscopy. *Nat. Commun.* 12:501.
38. Rothemund, P. W. 2006. Folding DNA to create nanoscale shapes and patterns. *Nature.* 440:297–302.
39. Stehr, F., J. Stein, …, P. Schwille. 2021. Tracking single particles for hours via continuous DNA-mediated fluorophore exchange. *Nat. Commun.* 12:4432.
40. Stehr, F., and J. Stein. 2021. picasso_addon. Version v1.0.2.
41. Chung, S. H., and R. A. Kennedy. 1991. Forward-backward nonlinear filtering technique for extracting small biological signals from noise. *J. Neurosci. Methods.* 40:71–86.
42. Mücksch, J., P. Blumhardt, …, P. Schwille. 2018. Quantifying reversible surface binding via surface-integrated fluorescence correlation spectroscopy. *Nano Lett.* 18:3185–3192.
43. Stehr, F., and J. Stein. 2021. lbFCS+. Version 1.0.0.
44. Edelstein, A. D., M. A. Tsuchida, …, N. Stuurman. 2014. Advanced methods of microscope control using μManager software. *J. Biol. Methods.* 1:e10.
45. Strauss, M. T., F. Schueder, …, R. Jungmann. 2018. Quantifying absolute addressability in DNA origami with molecular resolution. *Nat. Commun.* 9:1600.
46. McInnes, L., J. Healy, and S. Astels. 2017. hdbscan: hierarchical density based clustering. *J. Open Source Softw.* 2:205.
47. Huang, B., W. Wang, …, X. Zhuang. 2008. Three-dimensional super-resolution imaging by stochastic optical reconstruction microscopy. *Science.* 319:810–813.
48. Chung, K. K., Z. Zhang, …, J. Bewersdorf. 2020. Fluorogenic probe for fast 3D whole-cell DNA-PAINT. *bioRxiv* https://doi.org/10.1101/2020.04.29.066886.
49. Geertsema, H. J., G. Aimola, …, H. Ewers. 2021. Left-handed DNA-PAINT for improved super-resolution imaging in the nucleus. *Nat. Biotechnol.* 39:551–554.
50. Johnson-Buck, A., J. Li, …, N. G. Walter. 2019. A guide to nucleic acid detection by single-molecule kinetic fingerprinting. *Methods.* 153:3–12.
51. Chatterjee, T., A. Knappik, …, A. Johnson-Buck. 2020. Direct kinetic fingerprinting and digital counting of single protein molecules. *Proc. Natl. Acad. Sci. USA.* 117:22815–22822.
52. Qian, L., and E. Winfree. 2011. Scaling up digital circuit computation with DNA strand displacement cascades. *Science.* 332:1196–1201.
53. Cherry, K. M., and L. Qian. 2018. Scaling up molecular pattern recognition with DNA-based winner-take-all neural networks. *Nature.* 559:370–376.